PROCEEDINGS OF SCIENCE

In-situ Measurements of Ice Properties for the Radar Echo Telescope for Cosmic Rays

Contribution to ICRC 2025

Alexander Kyriacou[a,*] **on behalf of the Radar Echo Telescope collaboration**

[a] *Department of Physics and Astronomy, University of Kansas*
1251 Wescoe Hall Drive, Lawrence, KS, USA

E-mail: akyriacou@ku.edu

The upper 20 meters of the polar ice sheets exhibit significant density inhomogeneity. Understanding these ice effects on radio signal propagation is crucial for radio-based ultra-high-energy neutrino searches that use ice as a detection medium. We present in-situ measurements of density (ρ) and refractive index (n) in the upper 13 meters of ice at the Radar Echo Telescope for Cosmic Rays (RET-CR) site near Summit Station on the Greenland ice sheet, taken during the summer of 2024. The density was measured by assessing the mass and volume of extracted ice cores. The resulting ρ and n profiles are consistent with previous measurements at Summit. Additionally, a frequency-modulated continuous-wave signal was broadcast from an in-ice transmitter and measured at various depths inside a borehole. These signals were compared with simulations solving Maxwell's equations on a grid, using ice models derived from the in-situ ρ and n measurements.

39th International Cosmic Ray Conference (ICRC2025)
15–24 July 2025
Geneva, Switzerland

*Speaker

PoS(ICRC2025)313

1. Introduction

The radio transparency of polar ice, with attenuation lengths of $O(1\,\mathrm{km})$ [2], makes it an ideal medium for detecting ultra-high energy neutrinos (UHENs, $E_\nu > 10^{16}\,\mathrm{eV}$). Two detection methods are currently pursued: the first is the passive detection of *Askaryan* radio pulses generated by excess charge at the neutrino interaction site, using in-ice antenna strings or balloon-borne arrays [1, 4, 5]. The second is the radar echo technique, in which a transmitted pulse is scattered off the ionization trail left in the wake of the particle cascade [12]. In both cases, accurate modeling of RF signal propagation is essential for reconstructing the neutrino's properties [3]. RF signal propagation depends strongly on the ice's physical characteristics, namely the density, temperature, and the resulting refractive index profile. In the firn, where these properties vary rapidly with depth, small-scale fluctuations can significantly affect signal timing, amplitude, and fluence. Modeling this variability (especially seasonal changes) is crucial for reliable event reconstruction in large-scale UHE neutrino detectors.

The Radar Echo Telescope for Cosmic Rays (RET-CR) is a pathfinder experiment designed to test the radar echo method under natural conditions, using the upper Greenland firn as a target medium and cosmic rays as a test beam [12]. In the Arctic summer of 2024, the density and refractive index profile $n(z)$ of the upper 13 meters of firn at the RET-CR experimental site near Summit Station on the Greenland Ice Sheet were investigated using gravimetric measurements and radio sounding between boreholes via the Frequency Modulated Continuous Wave (FMCW) methods, the results of which are presented here.

2. RET-CR Setup and Calibration measurements

During the 2024 measurement campaign (May to August), the RET-CR detector was deployed in the configuration shown in the site survey map as shown in Fig. 1. The locations of all major components were recorded in a GNSS-RTK survey conducted on-site in May with a horizontal uncertainty of approximately 15 cm. The detector consisted of a central transmitter (TX) borehole, approximately 15 meters deep, which housed a phased array of eight transmitting antennas. This borehole defines the center of the detector array. Three additional boreholes, each 12 meters deep and containing a single receiver antenna (RX) at the bottom, were positioned in an approximate ring centered on the TX borehole with a radius of 30 meters. A fourth receiver borehole, referred to as the 'far borehole' was located 42 meters west of the TX borehole. All antennas were connected via coaxial cables to a central data acquisition system (DAQ) located at the surface near the TX borehole, with power supplied by a nearby horizontal photovoltaic (PV) array.

Within a 70-meter radius of the TX borehole, six surface stations were deployed. Each station consisted of two scintillator panels buried in the snow and a SKALA radio-frequency (RF) antenna [6]. The scintillator panels served as triggers for cosmic ray air shower events and also recorded cosmic ray event data independently of the RF system. To characterize the surface firn, including its density, a 13-meter-deep calibration borehole (denoted *CalBorehole*) was drilled using the Kovacs Mark V ice coring drill (also used for the other boreholes) [10]. Ice cores extracted from this borehole were used to determine the local density $\rho(z)$ and refractive index profile $n(z)$, described

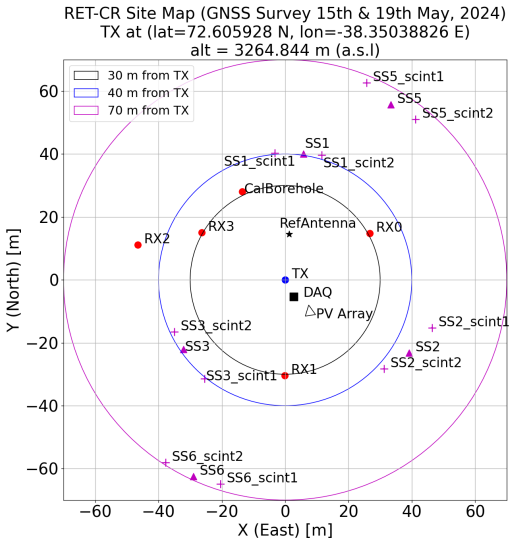

Figure 1: Map of the RET Site in the 2024 Arctic summer season. The locations were recorded in a GNSS survey (conducted by Curtis McLennan and the author of this work), and are plotted in a East-North-Up coordinate system.

below in section 3. In addition, both the calibration borehole and the far borehole were used to perform FMCW radio sounding measurements as described in section 4.

3. Density Measurements

The coring drill consisted of a 1-meter-long, 14 cm diameter barrel connected to a powered drill either directly or via a series of attached poles. It held each ice core in place using metal teeth commonly known as "dogs." Firn cores were extracted in increments of 50 - 80 cm and used to measure firn density as a function of depth via a simple gravimetric (i.e., weighing) method, where both the weight and volume of the core segment were recorded. To ensure a consistent conical volume for each measurement, each core was passed through a shaping apparatus, shown in Fig. 2, consisting of a metallic cylinder with an adjustable internal diameter, controlled via two metal strapping bands. The core was inserted into the cylinder and lightly compressed to remove surface extrusions, then pressed against a wooden board located 10 cm beyond the cylinder's exit. The exposed portion of the core was cut into a 10 cm segment using a serrated ice carving knife, and the trimmed ice was collected on a tray beneath.

The tray was then weighed using a set of digital scales with 1 g precision. While the core was pressed against the board, a coaxial probe embedded within the board made direct contact with the ice and measured the reflection coefficient at the core–probe interface. However calibration issues with this method lead to complications in the coaxial probe analysis and its result are not ready for presentation at the time of writing. Segments that contained cavities or were too fragmented to define a well-characterized volume were excluded from the density analysis.

The dominant source of measurement uncertainty was the weight loss during the cutting process, as small fragments of firn ("flakes") were often lost to the wind. To quantify this, a separate core

was extracted and weighed as a whole, then shaved, segmented, and weighed in the same fashion as the other samples. From the difference in total weight before and after processing, we estimated a mass uncertainty of $\delta m \sim 50\,\mathrm{g}$, which translates to a density uncertainty of $\delta\rho \sim 7\,\mathrm{kg/m^3}$.
In addition to the firn cores, two snow pit density measurements were conducted at the site near the "RefAntenna" location marked in Fig. 1. Snow samples were extracted from a vertical wall to a depth of 1.5 m using a [10 cm x 10 cm x 10 cm] wedge sampler, and weighed using the same set of 1 g precision scales. The two snow pits were located within 2 m of each other. The resulting RET

Figure 2: The core shaping rig: a metal cylinder of adjustable diameter used to trim the outer edges of firn cores to a consistent volume for gravimetric density measurements. The core is loaded into the rig from one side and pressed against a wooden board on the opposite side with a fixed gap. A 10 cm firn segment is shown being weighed on the tray below the apparatus.

density profile, measured to a depth of 13 m, is broadly consistent with previous measurements at Summit Station and surrounding sites. For comparison we take the density estimated using a Neutron-Scattering Probe (NSP) at Summit in 2006 and verified using simultaneous density and optical stratigraphy measurements [7, 8, 11]. An analytical fit to the RET site data was obtained using a broken exponential power law, with an inflection point at $\rho = 550\,\mathrm{kg/m^3}$:

$$\rho_{exp}(z) = \rho_i + (\rho_s - \rho_i)\exp(k \cdot z) \tag{1}$$

Where ρ_i is the density of ice, ρ_s is the surface density, and k is the densification constant, with $k = k_1$ for $\rho < 550\,\mathrm{kg/m^3}$ and $k = k_2$ for $\rho > 550\,\mathrm{kg/m^3}$. The best fit parameters to the RET data were: $\rho_s = 0.306 \pm 0.008\,\mathrm{g/cm^3}$, $k_1 = 0.0346 \pm 0.0014\,\mathrm{m^{-1}}$, and $k_2 = (19.6 \pm 0.7) \cdot 10^{-3}\,\mathrm{m^{-1}}$.
Fig. 3 compares the RET data to the NSP profile, and shows good agreement below 4 m depth, consistent with long-term stability of firn compaction at Summit. These outliers are evidence of surface melt events that occur sporadically in the Arctic summer, the melt-water percolating through the firn until reaching a depth at which they freeze and resulting in the formation of dense subsurface layers.
Above 4 m, larger variations appear among the RET, NSP, and snow pit measurements, indicating significant lateral variability in surface firn density. Most RET data points agree with the exponential fit to within a residual of $\Delta\rho = |\rho_{\mathrm{data}} - \rho_{\mathrm{fit}}| < 0.05\,\mathrm{g/cm^3}$. A single outlier in the RET data appears at $z = 3.5\,\mathrm{m}$ with $\Delta\rho > 0.15\,\mathrm{g/cm^3}$, and several comparable outliers are seen in the upper 2 m of Snow Pit 1.

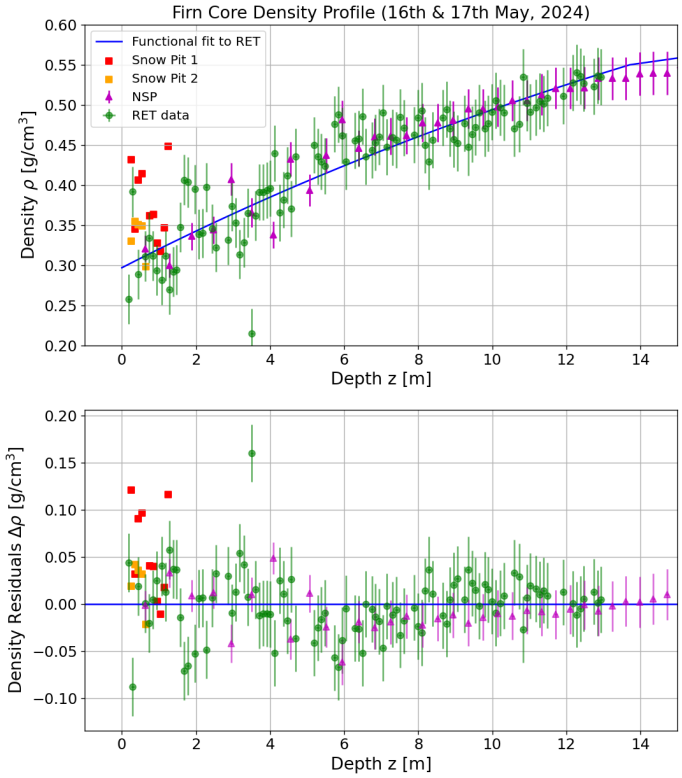

Figure 3: Top: Density profile of the upper 15 m of firn at Summit Station, Greenland. RET measurements (green points with error bars) are compared with snow pit measurements (Snow Pit 1 and 2) and a Neutron-Scattering-Probe (NSP) profile from [8]. A functional fit to the RET data is also shown. Bottom: Residuals of the density measurements relative to the fitted function.

4. Radio Propagation

We utilized RET's TX array to make direct measurements of a frequency-modulated continuous wave (FMCW) signal, transmitted from an antenna in the TX array and received by a set of four RX antennas, where one antenna was mobile and the remaining three were stationary (located at RX_0, RX_1, & RX_3 respectively). Each antenna corresponds to one of the four channels in the data acquisition system (DAQ), with the mobile antenna designated Ch2, and the stationary antennas assigned to Ch0, Ch1, and Ch3. A continuous wave signal $A(t)$ is broadcast with a linearly increasing instantaneous frequency $f(t)$. The frequency increases from a minimum to a maximum value over a modulation period T, with the bandwidth defined as $B = f_{\max} - f_{\min}$. The relative time delay $\Delta\tau$ between two FMCW signals $A_1(t)$ & $A_2(t)$ leads to an offset between their instantaneous frequencies f_1 & f_2. The multiplication of the two signals yields both the sum and the difference between f_1 & f_2, and after a lowpass we are left with the frequency offset Δf:

$$A_{\text{mix}}(t) = A_1(t)\sin(\omega(t)t) \cdot A_2\sin(\omega(t)(t+\tau)) \approx A_1A_2\cos(2\pi\Delta f(t)\cdot t). \tag{2}$$

Thus when the mixed FMCW signal A_{mix} is Fourier transformed, the resulting spectrum contains information about the relative propagation delay $\Delta\tau$ between the two channels. When the signal contains multi-path propagation, the individual signal paths are visible as peaks within the Fourier

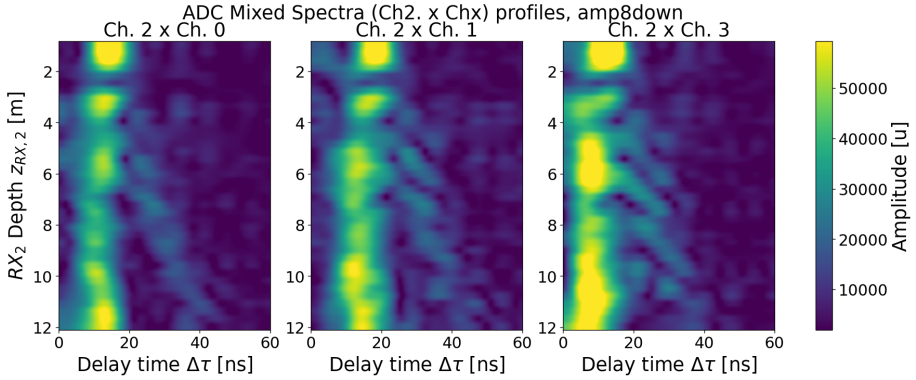

Figure 4: Mixed FMCW spectra between the mobile receiver antenna (Ch2) and the three stationary receivers (Ch0, Ch1, and Ch3), shown as heatmaps of relative signal amplitude as a function of delay time and depth. Each panel represents the beat signal resulting from the mixing of FMCW waveforms received at Ch2 and a stationary channel, with the mobile antenna incrementally lowered in 0.3 m steps. A bright vertical band located within 0 ns $\lesssim \Delta\tau \lesssim$ 20 ns corresponds to the direct trace, representing the direct signal path. A dimmer *reflection trace* emerges at depths below 4 m and diverges in delay time with increasing depth

spectrum. At each measurement depth, the FMCW signal is recorded on all four channels, with the mobile receiver RX_2 incrementally lowered in the borehole. Three FMCW profiles were recorded: two using the calibration borehole and one using the far borehole. The mobile receiver was stepped in 0.3 m intervals from the surface to the maximum depth and then raised again.

The resulting FMCW spectra for Ch2 mixed with Ch0, Ch1, and Ch3 are shown in Fig. 4 as distinct heatmaps, displaying the relative mixed-signal amplitude. Two prominent signal traces are visible in all three configurations: a bright *direct trace* near $\tau = 0$, corresponding to the direct signal path between TX and RX (within approximately 20 ns), and a dimmer *reflection trace* that separates from the direct trace at around $z = 4$ m and exhibits increasing delay with depth. All three channel combinations display a series of localized *hotspots*—enhanced RF amplitudes—at depths near 2 m, 6 m, and 10–11 m, likely corresponding to reflections from internal ice layers.

Differences in the spectral patterns between the three channel pairings provide further evidence of lateral variation in the firn structure. Spatial variations in firn density influence the local propagation conditions, resulting in different amplification patterns in each mixed-channel profile. These observations are consistent with lateral density inhomogeneities also seen in the density data, as seen in Fig. 3.

5. RF Simulation

In order to test the influence of the different density profiles on RF signal propagation at the RET site, the 3 density scenarios: 'NSP', 'RET' and 'analytical' are used to define the refractive index in RF propagation simulations of the detector. The parabolic equation (PE) method approximates wave propagation in a medium with refractive index $n(z)$ by assuming a time-harmonic scalar field $\psi \propto e^{i\omega t}$, governed by the Helmholtz equation:

$$\nabla^2\psi + k_0^2 n^2 \psi = 0, \tag{3}$$

where k_0 is the vacuum wave vector. Under cylindrical symmetry and paraxial (small-angle) propagation, a solution for a vertically polarized electric field $\hat{\mathbf{E}}(x, z, \phi) = E_z(x, z)$ is obtained, with x as the radial propagation coordinate [12]. Using the PE solver `paraProp`, we propagated RF emission from a TX phased array of 8 antennas located between 8 m and 14 m beneath the surface, throughout an ice medium of a depth 20 m and range of 50 m. The refractive index profiles were defined using the density profiles NSP, RET and analytical fit profiles as shown in fig 3 and using the empirical relation $n(z) = 1 + 0.845\rho(z)$ [9].

As an example, we show the RF emission amplitude $A_{RX}(f = 180\,\text{MHz})$ simulated using the RET-defined firn profile, as a function of depth z and horizontal range x, in Fig. 5a. Interference fringes and beam spreading appear as fan-like wavefronts radiating outward from the source, resulting from the complex refractive index gradient in the firn. Multiple dark notches and shadowed regions are the result of destructive interference due to internal layering.

To further illustrate the impact of firn structure, Fig. 5b shows the ratio of the RET-defined RF amplitude to that of an analytical reference model, $A_{\text{RET}}(f = 180\,\text{MHz})/A_{\text{fit}}(f = 180\,\text{MHz})$. The color map highlights dramatic deviations in RF amplitude arising from firn complexity. Red bands indicate enhanced RF amplitude relative to the analytical model, suggesting constructive interference, local focusing, or propagation paths reinforced by firn curvature or layering. Conversely, blue bands indicate signal suppression due to destructive interference, scattering, or shadowing effects, caused by the presence of relative dense layers throughout this region of the firn.

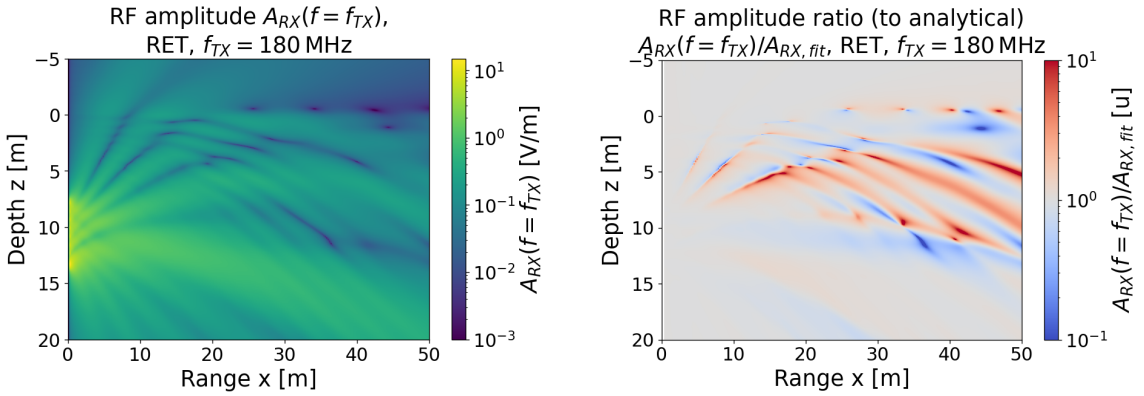

(a) **(b)**

Figure 5: Left (a): Heatmap showing 180 MHz RF emission amplitude from the TX phased array through the firn, as modeled by the RET density profile from Fig. 3.
Right (b) RF amplitude (at 180 MHz) ratio between ice defined by the RET density profile and the analytical fit.

6. Conclusions

The density measurements at the RET site near Summit Station, along with simultaneous radio frequency propagation measurements at the same location, demonstrate the complexity of the near-surface firn on relatively short scales, and that this leads to significant modulation of RF amplitude

traversing through the firn. Understanding these effects is vital for ensuring accurate reconstruction of neutrino and cosmic ray events using radio- and radar-based techniques.

References

[1] Abarr, Q., Allison, P., Ammerman Yebra, J. and et al. [2021], 'The payload for ultrahigh energy observations (pueo): a white paper', *Journal of Instrumentation* **16**(08), P08035.
URL: *http://dx.doi.org/10.1088/1748-0221/16/08/P08035*

[2] Aguilar, J. A., Allison, P., Besson, D. and et al [2022], 'Radiofrequency Ice Dielectric Measurements at Summit Station, Greenland', *arXiv e-prints* p. arXiv:2212.10285.

[3] Aguilar, J. A., Allison, P., Besson, D. and et al. [2023], 'Precision measurement of the index of refraction of deep glacial ice at radio frequencies at summit station, greenland'.
URL: *https://arxiv.org/abs/2304.06181*

[4] Allen, C., Bean, A., Besson, D. and et al [1998], 'Status of the radio ice cherenkov experiment (rice)', *New Astronomy Reviews* **42**(3), 319–329.
URL: *https://www.sciencedirect.com/science/article/pii/S1387647398000177*

[5] Askar'yan, G. A. [1961], 'Excess negative charge of an electron-photon shower and its coherent radio emission', *Zh. Eksp. Teor. Fiz.* **41**, 616–618.

[6] de Lera Acedo, E., Razavi-Ghods, N., Troop, N. and et al. [2015], 'SKALA, a log-periodic array antenna for the SKA-low instrument: design, simulations, tests and system considerations', *Experimental Astronomy* **39**(3), 567–594.

[7] Hawley, R. L. and Morris, E. M. [2006], 'Borehole optical stratigraphy and neutron-scattering density measurements at summit, greenland', *Journal of Glaciology* **52**(179), 491–496.

[8] Hawley, R. L., Morris, E. M. and McConnell, J. R. [2008], 'Rapid techniques for determining annual accumulation applied at summit, greenland', *Journal of Glaciology* **54**(188), 839–845.

[9] Kovacs, A., Gow, A. J. and Morey, R. M. [1995], 'The in-situ dielectric constant of polar firn revisited', *Cold Regions Science and Technology* **23**(3), 245–256.

[10] *Mark V Ice Coring System* [n.d.].
URL: *https://kovacsicedrillingequipment.com/product/mark-v-ice-coring-system/*

[11] Morris, E. M. [2008], 'A theoretical analysis of the neutron scattering method of measuring snow and ice density', *Journal of Geophysical Research: Earth Surface* **113**(F3).
URL: *https://agupubs.onlinelibrary.wiley.com/doi/abs/10.1029/2007JF000962*

[12] Prohira, S., de Vries, K., Allison, P. and et al [2021], 'The radar echo telescope for cosmic rays: Pathfinder experiment for a next-generation neutrino observatory', *Physical Review D* **104**(10).
URL: *http://dx.doi.org/10.1103/PhysRevD.104.102006*

Full Author List: RET Collaboration (June 28, 2024)

P. Allison[1], J.J. Beatty[1], D.Z. Besson[2], A. Connolly[1], A. Cummings[3,4,5], C. Deaconu[6], S. de Kockere[7], K.D. de Vries[7], D. Frikken[1], C. Hast[8], E. Huesca Santiago[7], C.-Y. Kuo[9], A. Kyriacou[2], U.A. Latif[7], J. Loonen[7], I. Loudon[10], V. Lukic[7], C. McLennan[2], K. Mulrey[10], J. Nam[9], K. Nivedita[10], A. Nozdrina[2], S. Prohira[2], J.P. Ralston[2], M.F.H. Seikh[2], R.S. Stanley[7], J. Stoffels[7], S. Toscano[11], D. Van den Broeck[7], N. van Eijndhoven [7], S. Wissel[4],

[1] Dept. of Physics, Center for Cosmology and AstroParticle Physics, The Ohio State University, Columbus, OH 43210
[2] Dept. of Physics and Astronomy, University of Kansas, Lawrence, KS 66045
[3] Center for Multi-Messenger Astrophysics, Institute for Gravitation and the Cosmos, Pennsylvania State University, University Park, PA 16802
[4] Dept. of Physics, Pennsylvania State University, University Park, PA 16802
[5] Dept. of Astronomy and Astrophysics, Pennsylvania State University, University Park, PA 16802
[6] Dept. of Physics, Enrico Fermi Institute, Kavli Institute for Cosmological Physics, University of Chicago, Chicago, IL 60637
[7] Vrije Universiteit Brussel, HEP@VUB, IIHE, Brussels, Belgium
[8] SLAC National Accelerator Laboratory, Menlo Park, California 94025, USA
[9] Dept. of Physics, Grad. Inst. of Astrophys., Leung Center for Cosmology and Particle Astrophysics, National Taiwan University, Taipei, Taiwan
[10] Department of Astrophysics/IMAPP, Radboud University, P.O. Box 9010, 6500 GL Nijmegen, The Netherlands
[11] Université Libre de Bruxelles, Science Faculty CP230, B-1050 Brussels, Belgium

Acknowledgements
We would like to acknowledge the following groups.

- The CODALEMA collaboration, for providing the surface radio DAQs used in RET-CR.
- The IceCube collaboration for providing the scintillator panels used for triggering RET-CR.
- The Summit Station staff for providing cargo logistics, warmth, food and much more.

We additionally recognize support from The National Science Foundation under Grants No. 2012980, No. 2012989, No. 2306424, and No. 2019597 and the Office of Polar Programs, the Flemish Foundation for Scientific Research FWO-G085820N, the European Research Council under the European Unions Horizon 2020 research and innovation program (Grant Agreement No. 805486), the Belgian Funds for Scientific Research (FRS-FNRS), IOP, and the John D. and Catherine T. MacArthur Foundation.